

An Elastically Gimbaled Z-Axis CMOS-MEMS Gyroscope

Hao Luo*, Gary K. Fedder** and L. Richard Carley*

*Department of Electrical and Computer Engineering and †The Robotics Institute
Carnegie Mellon University, Pittsburgh, PA 15213-3890
hluo@andrew.cmu.edu

Abstract

This paper presents a vertical (Z-axis) CMOS-MEMS gyroscope with a measured noise floor of $0.03^\circ/\text{sec}/\sqrt{\text{Hz}}$ and 1% linearity in the range of $-360^\circ/\text{sec}$ to $360^\circ/\text{sec}$. The gyroscope is fully compatible with conventional CMOS processes, which enable the integration of most of the conditioning circuits. It is fabricated in a three-metal-layer $0.5\mu\text{m}$ CMOS process followed by a two-step dry etch release. An improved out-of-plane curl matching technique provides the sidewall alignment to $1\mu\text{m}$. A new differential capacitive sensing interface is employed.

1. Introduction

Many automotive and consumer electronic applications require small, cheap angular rate sensors. Since the first micromachined silicon gyroscope was demonstrated ten years ago [1], many vibrating gyroscopes have been reported [2][3][4][5][6], where many of them require either vacuum packaging or multi-chip assembly.

A high-aspect-ratio CMOS micromaching process [7][8] developed at Carnegie Mellon University has advantages of 100% compatibility with conventional CMOS IC processes and multi-layer wiring. Using this process, one can make a fully integrated differential CMOS gyroscope. The integration of sensors and circuits suffers less parasitic capacitance and electrical noise pick-up. This process enables relatively high sensitivity and wide freedom in design.

However, the multi-layer microstructures in CMOS-MEMS experience curling during release. Out-of-plane curling may significantly decrease lateral sensing capacitance. Special consideration of curling control is required for proper function.

The first vertical gyroscope made in this process was reported in [5]. This paper will present a newly designed structure with decoupled modes. The second section briefly describes CMOS-MEMS process. The gyroscope structure design and the circuit design are presented in the third section. Test results and a summary are given in section 4 and section 5.

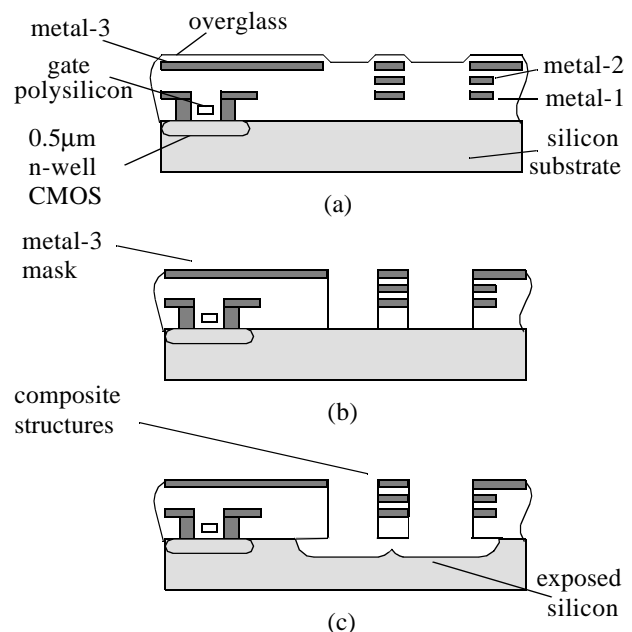


Figure 1: CMOS-MEMS process. (a) CMOS chip after fabrication (b) anisotropic RIE removes dielectric (c) isotropic RIE undercuts silicon substrate

2. CMOS Micromaching Process

The high-aspect-ratio CMOS micromaching technology [7][8] begins with a three metal $0.5\mu\text{m}$ n-well CMOS process. After the foundry fabrication, two dry etch steps, shown in Figure 1, are used to define and release the structure. Figure 1(a) shows the cross section of the chip after regular CMOS fabrication. In the first step of post processing (Figure 1(b)), dielectric layers are removed by an anisotropic CHF_3/O_2 reactive ion etch (RIE) with the top metal layer acting as an etch resistant mask. After the sidewall of the microstructure is precisely defined, an isotropic SF_6/O_2 RIE is performed to etch away the bulk silicon and release the structure (Figure 1(c)). Multi-layer conductors can be built in the composite structure, which enables more flexible designs than homogeneous conducting structures.

The undercut of silicon in the release step (Figure 1(c)) requires the placement of sensing circuits to be at least $40\mu\text{m}$ away from the microstructures. Compared to commercial polysilicon micromaching technology, the CMOS-MEMS clearance is smaller and suffers less parasitic capac-

itance. Such parasitics are to be avoided when a capacitive sensing technique is applied.

3. Gyroscope Design

3.1. Sensor Design

The principle of vibratory gyroscope comes from the Coriolis force in a non-inertial rotating system. When rotation Ω is applied, a moving object with mass m and velocity v experiences a Coriolis force $2m\Omega \times v$. Thus by detecting this Coriolis force, the rotation is measured.

The presented gyroscope is composed of an accelerometer nested in a movable rigid frame (Figure 2). An outer actuator drives the rigid frame in one lateral direction (X-axis), and the inner accelerometer measures the orthogonal deflection due to the Coriolis force (Y-axis).

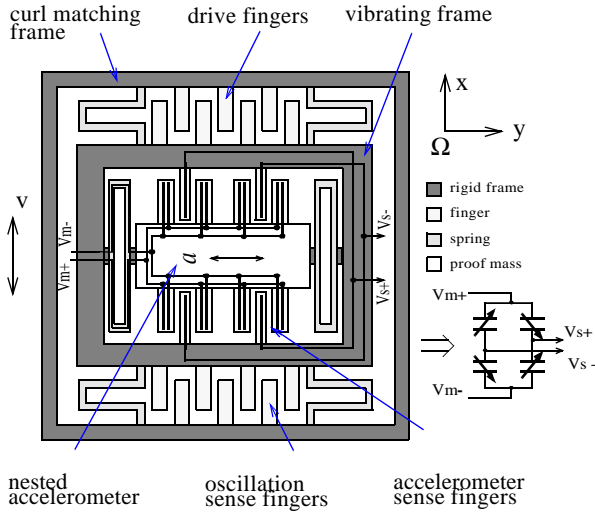


Figure 2: Schematic of gyroscope and inner sensing equivalent model.

The elastically gimbaled structure completely decouples the Coriolis sense mode from the vibration drive mode[5]. The modulation clock and sensing signals of the inner accelerometer are routed through the multi-layer springs. One set of comb fingers on the outer rigid frame generates the electrostatic force for vibration, while the comb fingers on the opposite side sense the movement of the vibrating frame to sustain the oscillation.

The nested accelerometer uses the same topology described in [9]. It is a fully differential common-centroid accelerometer with sensing fingers attached at the inner rigid frame. In the layout, each half-capacitive bridge is split into two parts and located at two cross-axis corners. This common-centroid layout topology cancels common-mode input noise such as substrate coupling, power supply coupling and cross-axis vibration.

By taking advantage of multi-layer routing, a set of actuators is incorporated on the accelerometer to cancel the offset due to fabrication variation. To avoid cross-axis actuation, the actuator is partitioned into four parts and symmetrically located at each corner of the accelerometer (Figure 3). Differential force fingers are biased with the power supply voltages, V_{dd} & V_{ss} .

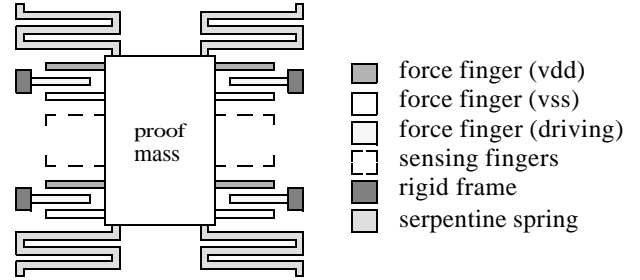


Figure 3: Offset cancellation actuator

The composite CMOS-MEMS structure experiences larger vertical stress gradients than its polysilicon counterpart [10]. Out-of-plane curling significantly reduces the sidewall capacitance which is critical to capacitive sensing. To solve this problem, fingers on the stator are attached to a rigid frame (Figure 4) instead of to the substrate. The rigid frame is anchored along a common axis with the proof mass, and is subjected to the same stress gradient as the inner structure. Thus a first-order curl matching is achieved. To get optimal matching, the middle part of the rigid frame is designed to have the same density of holes in its structure as the proof mass. The outer part of the rigid frame is composed of beams which are similar to the fingers. This design reduces the pattern sensitive mismatch between the inner and outer structures.

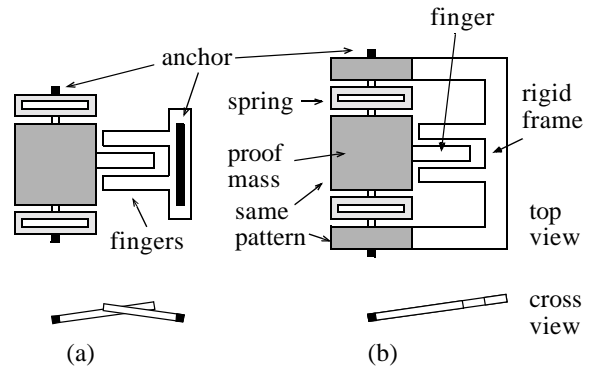


Figure 4: Local curl matching technique (a) Without curl matching. (b) With curl matching

The gyroscope design was simulated in Cadence SPECTRE™ using NODAS [11]. The simulation schematic is given in Figure 5. Some key parameters are given in Table 1.

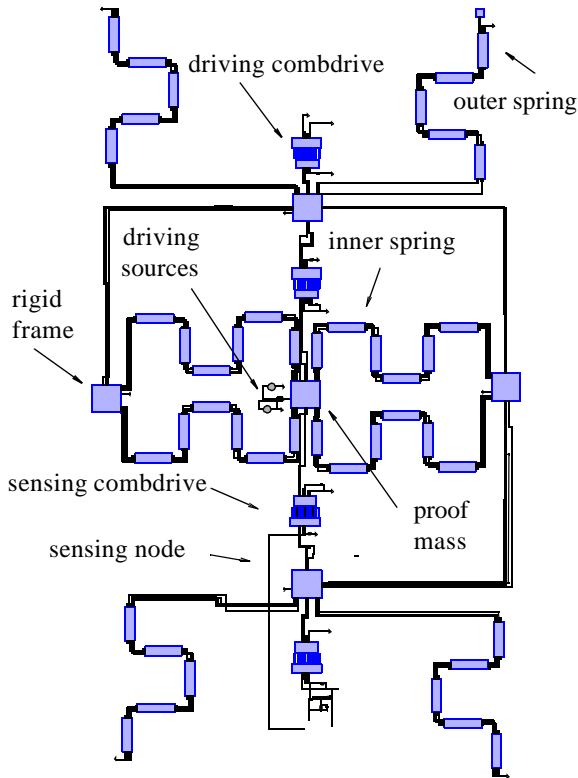


Figure 5: Sensor simulation schematic

Table 1. Layout parameters of the gyroscope

device size	360 μm \times 500 μm
proof mass size	116 μm \times 372 μm
sense comb finger	61.5 μm \times 3.9 μm
drive comb finger	11.4 μm \times 2.7 μm
finger gap	1.8 μm
sense finger number	44
drive finger number	23
outer spring beams	1.8 μm \times 105 μm
inner spring beams	1.8 μm \times 128 μm

The asymmetric design between the X and Y axis results in driving and sensing modes with unmatched resonant frequencies. In contrast to matched-mode vibratory-rate gyroscopes, the nested-accelerometer gyroscope has a gain that it is insensitive to the drift in the resonant frequencies. The simulation (Figure 6) shows that the driving mode resonant frequency 9.5kHz is lower than the sensing mode resonant frequency 11.3kHz. Thus, even with fabrication variation, the sensitivity of the inner accelerometer will not be significantly attenuated by the second-order slope at frequencies higher than its peak. Since the unmatched mode

design does not rely on the gain of quality factor Q and its narrow bandwidth, the sensitivity variation due to frequency drift is decreased.

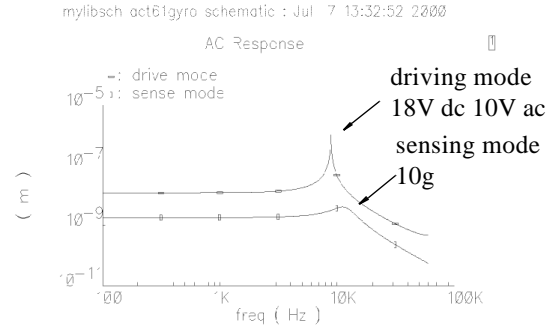


Figure 6: Two modes of gyroscope

3.2. On-chip Sensing Circuit Design

The on-chip fully differential sensing amplifier (Figure 7) detects the capacitance change due to deflection of the comb fingers. A cascode stage is employed to reduce the input capacitance. Since the system noise level is dominated by the first stage, the input stage with large gain is essential to the system performance. Simulation shows this input amplifier has a gain of 80 and bandwidth of 10MHz with 10pF capacitance load. The input biasing problem of the capacitive sensing interface is solved by using two small transistors (m3, m4, W/L=2.4 μm /2.1 μm) working in the subthreshold range. These two transistors exhibit large resistance and no source to drain capacitance. This technique eliminates the requirement of large resistors which are not feasible in the CMOS process.

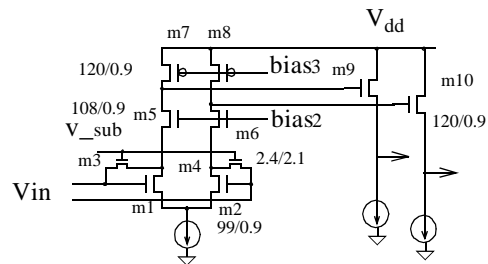


Figure 7: Capacitive sensing circuit

To avoid the damage caused by undercut of silicon in the RIE (see Figure 1 (c)), all circuits are put 40 μm away from the sensor. Except for the microstructure, the entire chip area is covered by the top metal layer.

Figure 8 shows a block diagram of the complete system. An off-chip high voltage amplifier drives the top combdrive to sustain the vibration while the signal from inner accelerometer is demodulated twice to recover the rotation signal.

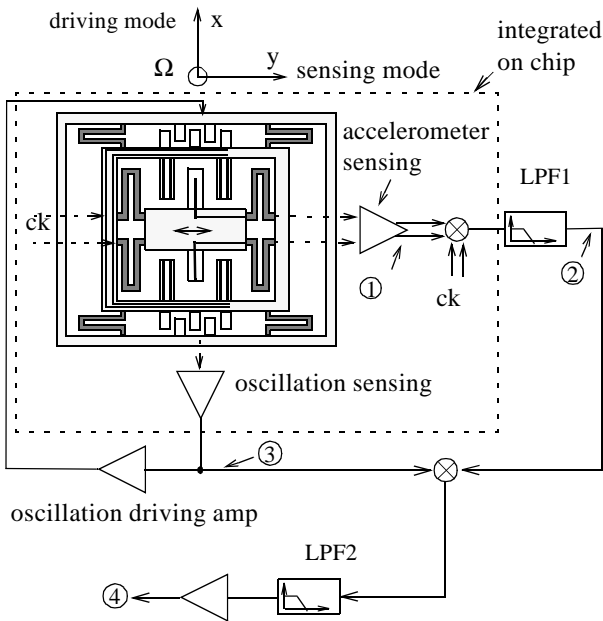


Figure 8: Block diagram of gyroscope system.

4. Experiments

The device was fabricated in the Hewlett-Packard three-metal 0.5 μm n-well CMOS process. Figure 9 shows the SEMs of the released CMOS-MEMS gyroscope.

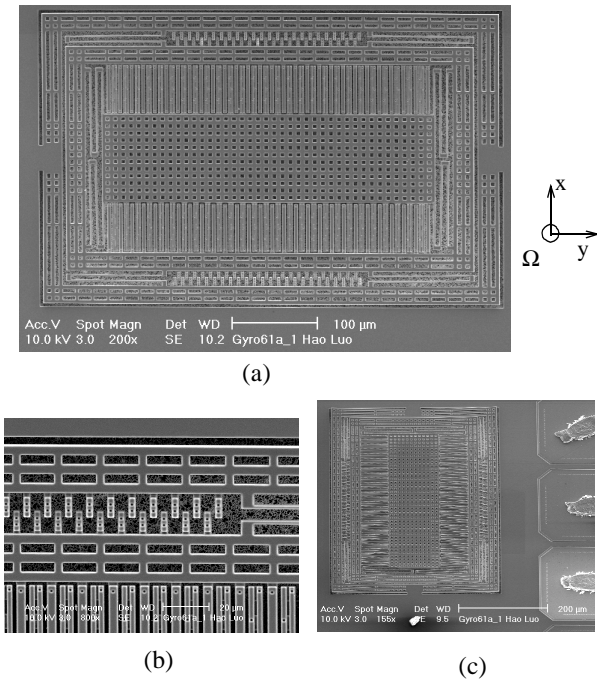


Figure 9: (a) SEM of the gyroscope. (b) Comb fingers and rigid frame. (c) Out-of-plane curl.

The driving mode three-axis motions of the gyroscope are first studied using the MIT Microvision™ system [12] to quantify the coupling between the driving mode and sensing mode. An 18V dc plus 10V ac signal was applied to the outer driving comb fingers. As can be seen from Figure 10, the vibratory part gets maximum motion in the X-axis (lateral) direction at the resonant frequency 9.2kHz with a Q of 120, while the Y-axis motion maintains low level in the full frequency range. The decoupled modes between X-axis and Y-axis makes the vibrating accelerometer move in a straight line in the lateral plane. The X-axis motion slightly couples into the Z-axis motion (Figure 10). Two reasons may account for the coupling. (a) Due to the slightly mismatched comb fingers, a lift force is generated. During the lateral motion, the more the combdrive finger is engaged, the larger the lift force is. Thus the lateral (X-axis) movement is accompanied with a small Z-axis motion. (b) The inevitable mounting error causes the sample not perpendicular to the measurement light beam. Then the motion can be decomposed into two vectors in the X-axis and Z-axis, and results in the observed Z-axis motion.

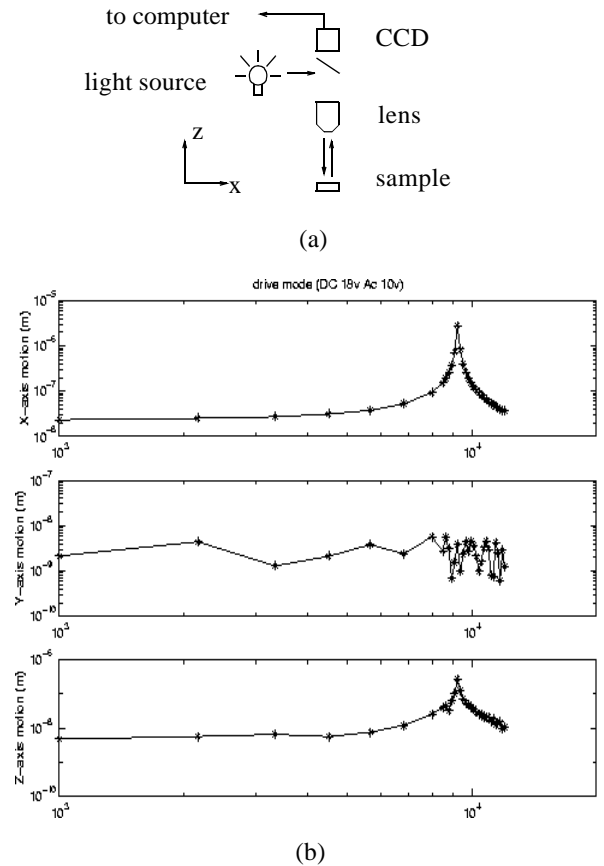


Figure 10: (a) Microvision system and (b) Gyroscope three axis motions in driving mode.

The motions when driven in the sensing axis are also measured to check the resonant frequency in the sensing

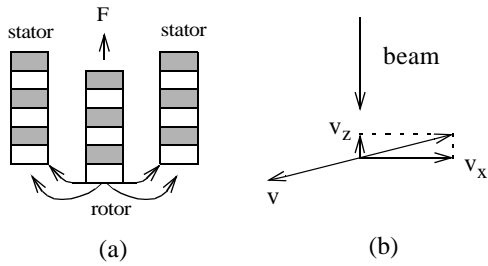


Figure 11: Mode coupling mechanism. (a) Electrostatic lift force (b) Misalignment coupling

mode. This is done by applying a 9V dc plus 3V ac signal to the actuator on the accelerometer.

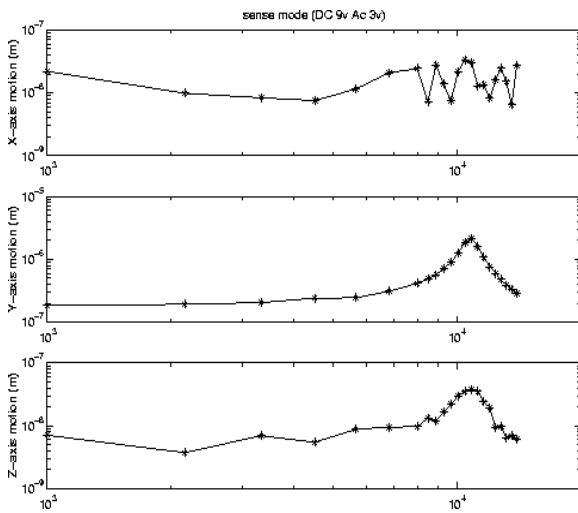


Figure 12: Three axis motion in sensing mode.

Figure 12 shows the sensing mode resonant frequency (Y-axis) is 11kHz, which also matches the simulation very well. As can be seen, the sensing mode has a smaller Q of 12. This is because the nested accelerometer has more lateral fingers than the outer driving non-lateral fingers, and the squeeze damping between those lateral fingers is larger than the Couette damping of the outer counterparts.

The dynamic measurement setup (Figure 13) consists of an AeroSmith 1270VS rate table, a HP 4395A spectrum analyzer, and a LeCroy 9354L digital oscilloscope.

Figure 14 shows the waveforms of the gyroscope captured at the nodes shown in Figure 8 when 180°/sec rotation is applied.

Figure 15 shows the linearity of the gyroscope in a range of -360°/sec~360°/sec. The gyroscope equivalent noise floor is $0.03^\circ/\text{sec}/\sqrt{\text{Hz}}$.

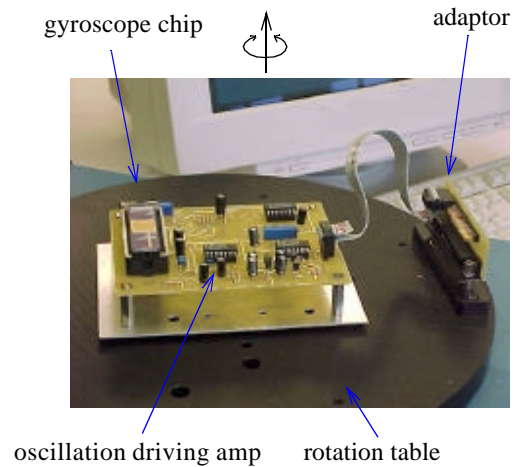


Figure 13: Gyroscope on a rotation table.

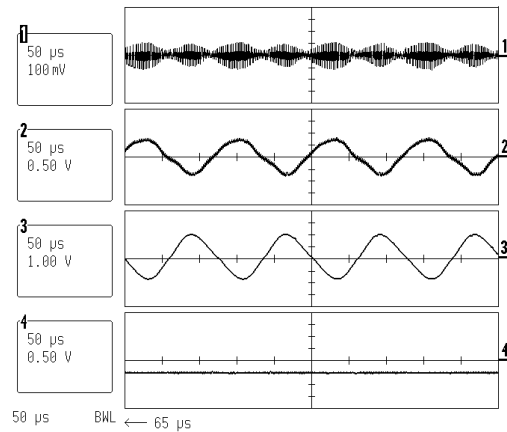


Figure 14: Waveforms captured at nodes in Figure 8. (refer to Figure 8)

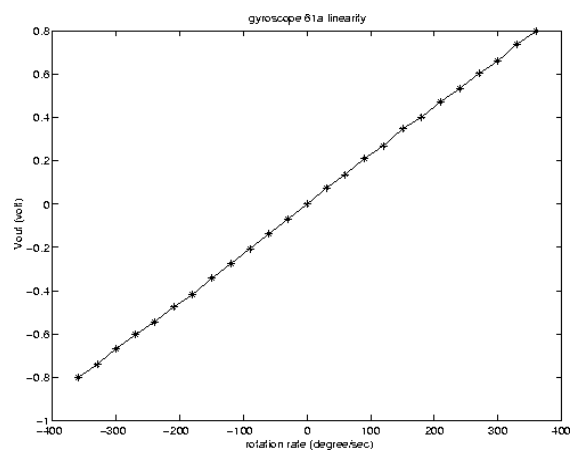


Figure 15: Gyroscope output linearity

Table 2 summarizes the test results of this gyroscope.

Table 2: Technical Data of gyroscope

Parameter	Measured result
On-chip circuit power supply voltage	5 V
Vibration Drive voltage	DC=24 V, AC=10 V
Working ambient	760 Torr
Driving mode resonant frequency	9.2 KHz
Sensing mode resonant frequency	11 KHz
Sensitivity	2.2 mV/°/sec
Noise (over 20 Hz BW)	0.03°/sec/ $\sqrt{\text{Hz}}$
Linearity (-360~360 °/sec)	1%

5. Conclusion

A functional vertical vibratory rate gyroscope has been realized in a CMOS-MEMS process. Using the decoupled mode design, the gyroscope does not rely on the gain of Q by matching modes. The ambient pressure is not critical to its function. Simulation verification is important to design the two mode resonant frequencies in the right order.

Acknowledgment

The authors would like to thank Q. Jing for the NODAS simulation. This work is supported by Defense Advanced Research Projects Agency, Air Force Materiel Command, USAF, under agreement F30602-97-2-0323.

References

[1] Greiff, B.Boxenhorn, T. King, and L. Niles, "Silicon

Monolithic Gyroscope," *Transducers91, Digest of Technical Papers*, pp. 966-969,1991 International Conference on Solid State Sensors and Actuators, IEEE Cat. #91CH2817-5, June 24,1991.

- [2] W. A. Clark, R. T. Howe, "Surface micromachined Z-axis vibratory rate gyroscope," *Solid state Sensor and Actuator workshop 96* pp. 283-287, Hilton Head, SC
- [3] S.S. Beak, Y.S. Oh, B.J. Ha, S. D. An, B.H. An. Song, C.M. Song, "Asymmetrical Z-axis gyroscope with a high aspect ratio using simple and new process," *MEMS 99*, pp. 612-617
- [4] W. Geiger, B. Folkmer, J. Merz, H. Sandmaier, and W. Lang, "A new silicon rate gyroscope," *MEMS 98*, Heidelberg, Germany, Feb. 1998, pp. 615-620
- [5] M. S. Kranz and G. K. Fedder, "Micromechanical Vibratory Rate Gyroscopes Fabricated in Conventional CMOS," *Proc. Symposium Gyro Technology*, Stuttgart, Germany, September 16, 1997, pp. 3.0-3.8.
- [6] E. J. J. Kruglick, B. A. Warneke, and K. S. J. Pister, "CMOS 3-Axis gyroscopes with Integrated Amplifier," in *Proc. of IEEE MEMS Workshop*, Heidelberg, Germany, Jan. 25-29, 1998, pp. 631-636.
- [7] G.K.Fedder, S.Santhanam, M.L.Reed, S.C.Eagle, D.F.Guillou, M.S.-C.Lu, and L.R.Carley, "Laminated high-aspect-ratio micro-structures in a conventional CMOS process," *Sensors and Actuators*, v.A57, no. 2, pp. 103-110.
- [8] X.Zhu, D.W.Greve., R.Lawton, N.Presser, and G.K.Fedder, "Factorial Experiment on CMOS-MEMS RIE Post Processing," in *Proc. of the 194th Electrochemical Society Meeting, Symposium on Microstructures and Microfabricated Systems IV*, vol. 98-14, Boston, MA, Nov. 1-6, 1998, pp.33-42
- [9] Hao Luo, G.K.Fedder and L. Richard Carley, "A 1 mg CMOS-MEMS Lateral Accelerometer," *MEMS 2000 Miyazaki*, Japan, pp502-507
- [10] M.S.-C.Lu, X.Zhu, and G.K.Fedder, "Mechanical Property Measurement of 0.5 μm CMOS Microstructures," in *Proc. of the Material Research Society (MRS) 1998 Spring Meeting, Symposium on Microelectromechanical Structures for Materials Research, San Francisco, CA*, Apr. 13-17, 1998.
- [11] G. K. Fedder and Q. Jing, "A Hierarchical Circuit-level Design Methodology for Microelectromechanical Systems," *IEEE Tran. on Circuits and Systems II: Analog and Digital Signal Processing*. Oct. 1999, vol. 46, no. 10. pp. 1309-1315
- [12] MIT Microvision™ manual guide